

# Fine Robotic Manipulation without Force/Torque Sensor

Shilin Shan<sup>1,\*</sup>, and Quang-Cuong Pham<sup>2</sup>

**Abstract**—Force Sensing and Force Control are essential to many industrial applications. Typically, a 6-axis force/torque (F/T) sensor is installed between the robot’s wrist and the end effector to measure the forces and torques exerted by the environment on the robot (the external wrench). While a typical 6-axis F/T sensor can offer highly accurate measurements, it is expensive and vulnerable to drift and external impacts. Existing methods aiming at estimating the external wrench using only the robot’s internal signals are limited in scope. For instance, the estimation accuracy has mainly been validated in free-space motions and simple contacts, rather than tasks like assembly that require high-precision force control. In this paper, we present a Neural-Network-based solution to overcome these challenges. We offer a detailed discussion on model structure, training data categorization and collection, as well as fine-tuning strategies. These steps enable precise and reliable wrench estimations across a variety of scenarios. As an illustration, we demonstrate a pin insertion experiment with a 100-micron clearance and a hand-guiding experiment, both performed without external F/T sensors or joint torque sensors.

**Index Terms**—Machine Learning for Robot Control, Industrial Robots, Dynamics, Model Learning for Control

## I. INTRODUCTION

**F**ORCE sensing and force control are essential in various industrial applications, from contact-based inspection to assembly, sanding, deburring, and polishing [1]–[3]. Typically, a 6-axis force/torque (F/T) sensor is installed between the robot’s wrist and the end-effector to measure forces and torques (the external wrench) applied by the environment to the robot. Although a standard 6-axis F/T sensor offers highly accurate measurements, it is expensive and vulnerable to drift and external impacts. Consequently, there has been substantial research geared towards estimating the external wrench using solely the robot’s internal signals, such as joint position, joint velocity, or motor current readings.

To that aim, there are two main approaches in the literature: model-based and model-free. The model-based approach constructs parameterized models of the robot’s dynamics, which are then identified using standard parameter identification techniques [4]–[7]. However, the precise modeling and identification of highly nonlinear and nonsmooth phenomena,

Manuscript received: July 21, 2023; Revised September 26, 2023; Accepted December 06, 2023.

This paper was recommended for publication by Editor Hyungpil Moon upon evaluation of the Associate Editor and Reviewers’ comments.

<sup>1</sup> Shilin Shan is with School of Mechanical and Aerospace Engineering, Nanyang Technological University, Singapore. e-mail: shilin.shan153@gmail.com

<sup>2</sup> Quang-Cuong Pham is with Eureka Robotics and Singapore Centre for 3D Printing (SC3DP), School of Mechanical and Aerospace Engineering, Nanyang Technological University, Singapore. e-mail: cuong@ntu.edu.sg

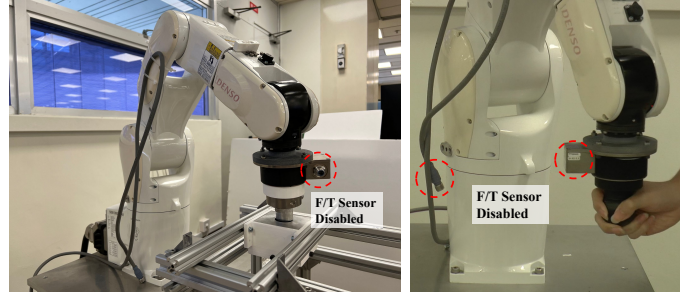


Fig. 1: Snapshot of the sensorless tight pin insertion and hand-guiding experiment setup. Video demonstrations of the experiments in Section VI is available in the supplementary materials or at: <https://youtu.be/spztx3GzPzc>

such as hysteresis and joint friction in low-speed areas, pose considerable challenges. To address these and simplify the modeling process, model-free methods based, e.g., on Gaussian Process Regression and Neural Networks (NN), have been developed in [8]–[10]. Nevertheless, these methods have a limited scope. Specifically, the accuracy of wrench estimation has predominantly been validated in scenarios involving only free-space motions and straightforward contacts. It has not been extensively tested in complex industrial tasks demanding high-precision force control.

Here, we present a NN-based method and argue that the aforementioned challenges can be addressed by specifically focusing on the training data and NN structure. We highlight the importance of collecting and classifying data for both free-space and in-contact motions in the low-speed scenarios, while also selecting a model that balances simplicity and accuracy. The main contributions can be summarized as follows:

- We investigated systematically the estimation accuracy and computational cost of various NN structures. The findings offer valuable insights into selecting the optimal model structure for wrench estimation and hopefully similar regression tasks across different applications.
- We introduce a unique training strategy that initially trains a base model using unbiased data, followed by fine-tuning to enhance performance in contact-rich applications. The training data were collected through a combination of free-space motion planning, high-precision force control, and physical human-robot interaction tasks.

We demonstrate a pin insertion experiment with 100-micron clearance and a hand-guiding experiment, both conducted without the use of F/T sensors during runtime. Notably, an F/T sensor is still required for the one-time data collection during the training phase. For expansive industrial applications, a well-trained Neural Network can be ported to other

manipulators of the same model with suitable transfer learning strategies [11].

The structure of the paper is as follows: Section II offers an overview of literature related to both model-based and model-free wrench estimation. In Section III, we introduce the implementation of the model-based scheme and NN structures. Section IV elaborates on data collection methodologies and provides a detailed procedure. Section V presents the model training outcomes and delves into the principles of model selection, considering dataset coverage. Section VI showcases four experiments performed in both free-space and in-contact situations. Fig. 1 provides a snapshot from the sensorless pin insertion and hand-guiding experiments.

## II. RELATED WORK

Early research introduced a systematic approach to dynamics identification and trajectory excitation [12]. Following this, the renowned Generalized Momentum Observer (GMO) [4], [13] was proposed, aiming to derive high-quality torque residual estimates based on either driving torque or current measurements. While mathematical analyses offer crucial insights into rigid body dynamics, approximating joint frictions in low-speed scenarios is challenging. These scenarios might encompass highly nonlinear phenomena, such as hysteresis [14]. Beyond the conventional friction models addressing Coulomb friction, stiction, viscous friction, and Stribeck friction [15], alternative methods have been suggested. These methods aim to mitigate friction errors by employing sigmoid functions [16], [17] or the Kalman Filter [6]. Recent studies have also put forth semi-parametric approaches that utilize Neural Network models to learn joint motor friction [9] and counteract non-modeled effects [18]. Despite the in-depth error analyses provided, the robustness of these methods in high-precision practical applications remains to be ascertained.

Another approach is to bypass manual selection of the entire model structure and instead allow the model to learn from one-time data collection. Early research has explored non-parametric regression-based approaches for model identification [19], [20]. Building upon these methods, several studies have demonstrated the ease of training non-parametric learning-based approaches such as Gaussian Process Regression (GPR) and Locally Weighted Projection Regression (LWPR) [8], [21], [22]. By avoiding manual selection of the model structure, regression-based approaches eliminate human bias and enable the model to learn the optimal structure given simple hyperparameters. GPR, which has been trained and validated using hand-guiding experiments [8], exhibits high accuracy in trajectory tracking. However, this task alone may not adequately represent contact-rich industrial tasks. Additionally, as discussed in Section III, the hand-guiding dataset may be biased due to the strong correlation between end-effector force and motion.

Following Section I, we propose the use of Neural Networks to avoid complex mathematical modeling while ensuring estimation accuracy. Neural Networks have proven to be effective in approximating nonlinear mappings in various domains. Recent research has applied different Neural Network structures

to various industrial tasks. For example, Multilayer Perceptron (MLP) has been proposed in [10], [11], [23] for Inverse Dynamics Identification and contact detection by classifying the robot motion status. Convolutional Neural Networks (CNN) have been utilized in [24], [25] to estimate external forces by detecting the physical deformation of objects. Recurrent Neural Networks (RNN), particularly Long Short-term Memory Networks (LSTM), have been proposed in [26], [27] for robot tracking and hysteresis approximation. In general, MLP provides a direct nonlinear mapping from the input to the output. CNN and LSTM, on the other hand, are specialized in extracting specific features from input data and capturing temporal information [28], respectively.

In this paper, we evaluate the performance of MLP, CNN, and LSTM in the wrench estimation task and demonstrate that MLP can achieve more accurate estimation given equal inference time. In Section VI, we compare the fine-tuned MLP with the model-based method - implemented following standard dynamics identification procedure [12], the GMO scheme proposed in [16], and the friction compensation techniques discussed in [6], [17].

## III. PRELIMINARIES

### A. Model-based Identification

Consider a robot with rigid joint, the robot dynamics can be described as follows:

$$M(q)\ddot{q} + C(q, \dot{q})\dot{q} + g(q) + \tau_f(\dot{q}) = \tau_{motor} + \tau_{ext} \quad (1)$$

where  $M(q)$ ,  $g(q)$ ,  $\tau_f(\dot{q})$ ,  $\tau_{motor}$ ,  $\tau_{ext}$  are the inertia matrix, Gravity vector, joint friction, motor driving torque, and external torque, respectively.  $C(q, \dot{q})$  is the factorized Coriolis matrix such that  $\dot{M} - 2C$  is skew-symmetric. Such a property enables the design of a Generalized Momentum Observer (GMO) [4] that avoids the use of noisy acceleration, being described by the following equation:

$$r(t) = L \left( M(q)\dot{q} - \int_0^t (\bar{\tau} + r) ds \right) \quad (2)$$

where  $r$  is the approximated residual,  $L$  is the diagonal gain matrix, and  $\bar{\tau} = C^T(q, \dot{q})\dot{q} - g(q) - \tau_f(\dot{q}) + \tau_{motor}$ . Considering a setting where only current measurements are available, dynamics parameter identification can be conducted on the current level using the following equation:

$$Y(q, \dot{q}, \ddot{q})\hat{\pi} = I \quad (3)$$

where  $Y$ ,  $\hat{\pi}$ ,  $I$  are the regressor matrix, dynamics parameters, and motor current vector, respectively. The exciting trajectory proposed in [17] was considered for data collection. A standard pseudoinversion was used for identification:  $\hat{\pi} = \bar{Y}^\# \bar{I}$ , where  $\bar{Y}$  is the stacked regressor matrix evaluated with the collected data, and  $\bar{I}$  is the stacked current measurements.

The end-effector wrench can be approximated using:

$$F = (J^T)^\# K I \quad (4)$$

where  $F$ ,  $J$ ,  $K$  denote the external wrench, the geometric Jacobian and the diagonal motor constant matrix. However, the motor constants are not available for our robot model. Supplementary experiment was conducted, calculating external

joint torques with wrench measurements, thereby approximating the motor constant with the estimated current residuals from equation (2).

Notably, we used a friction model discussed in [6]:

$$\tau_f(\dot{q}_i) = \left( (C_{C,i} + C_{S,i} \cdot e^{-\left(\frac{\dot{q}_i}{v_{S,i}}\right)^2}) \text{sgn}(\dot{q}_i) + C_{V,i} \cdot \dot{q}_i \right) \quad (5)$$

where  $i$  denotes the  $i^{\text{th}}$  joint,  $C_{C,i}$ ,  $C_{S,i}$ ,  $C_{V,i}$ , and  $v_{S,i}$  are the coefficient for Coulomb friction, stiction, viscous friction and Stribeck friction, respectively. Identified large Coulomb coefficients can induce high-frequency oscillations in estimations when  $\dot{q}$  approaches zero. To enable a smooth transition around this zero velocity, a Sigmoid function is employed [17]:

$$\tau_{fC,i} = \frac{\varphi_{1,i}}{1 + e^{-\varphi_{2,i}(\dot{q}_i + \varphi_{3,i})}} - \frac{\varphi_{1,i}}{1 + e^{-\varphi_{2,i}\varphi_{3,i}}} \quad (6)$$

where  $\tau_{fC,i}$  can replace the  $C_{C,i} \cdot \text{sgn}(\dot{q}_i)$  term in equation (5), and  $\varphi_{1,i}$ ,  $\varphi_{2,i}$ , and  $\varphi_{3,i}$  are the parameters to be identified. Despite handling friction terms carefully in the low-speed scenario, this implementation still shows inaccuracies in the applications discussed in Section VI, especially in static scenarios where hysteresis is observed to be a prominent issue.

### B. Neural Networks Model Structure

The model structures of MLP, LSTM, and CNN implemented and used for comparisons are shown in Fig. 2.

1) *MLP*: The model takes each frame of joint currents and states, including position, velocity, and acceleration, as input and maps them to the end-effector wrench. The training time, inference time, and estimation accuracy are highly influenced by the network depth and hidden layer size. The relationship between these hyperparameters and the coverage of the training set will be discussed in Section V.

2) *LSTM*: The recurrent structure of the model comprises one fully-connected (FC) layer, two LSTM layers, and another FC layer. It takes in one frame of joint currents and states and estimates the wrench for the same frame. The latent information, represented by the hidden states  $h_n$  and cell states  $c_n$ , is then propagated to the subsequent LSTM layers for the next frame. This process enables the model to learn from both long-term and short-term joint state memories [26], [27]. Further information regarding the related theory and the detailed structure of the LSTM layer can be found in [29].

3) *CNN*: The model typically receives 2D images as input, enabling it to understand the pixel relationships and extract relevant features. In the case of joint currents and states as input, the data pattern is adapted to a CNN by concatenating the current data frame with multiple previous frames, forming a 2D matrix. The convolutional kernel is designed to extract features from individual input frames as well as across multiple frames. A similar idea can be found in [30], where CNN was used for identifying the features across dynamics equation and friction components. Additional information about the related theory and convolution process can be found in [31].

4) *Training Framework*: We implemented the models and data loader, then trained the models with PyTorch. The loss function and optimization method are MSEloss and Adam Optimizer, respectively. ReLU activation was applied to all FC

and convolutional layers, while Sigmoid and tanh were used as the default activation functions for LSTM layers. Detailed information about the hyperparameters will be discussed in Section V along with the training data.

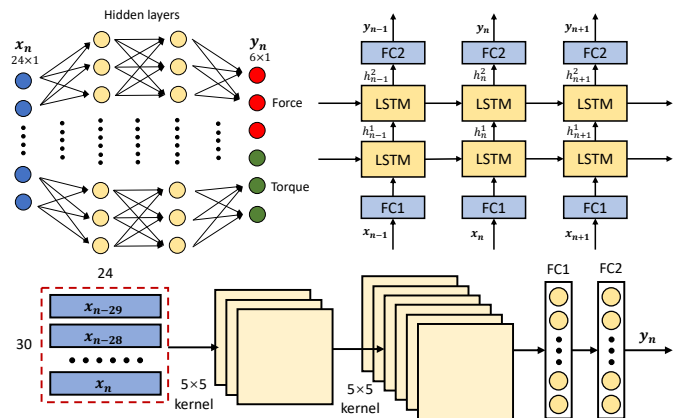


Fig. 2: The model structure of MLP (top left), LSTM (top right) and CNN (bottom) implemented for wrench estimation

## IV. TRAINING DATA GENERATION

In this section, we introduce a unique data collection method, grounded in the concepts of dynamics information bias and the strategy of problem-solving fine-tuning.

### A. Fundamental Concepts

For the model-based approach, we can adopt the method outlined in [17], using conventional sinusoid trajectories excited in the joint space. The well-defined robot dynamics enables straightforward parameter fitting with minimal training data, made possible through optimized trajectory design. Conversely, for the NN-based approach, there are no prior assumptions, meaning the learning result depends entirely on the training data distribution. In response, we introduce a data collection scheme designed to encompass a broad range of scenarios. Specifically, we segment the training data into two categories: a base dataset and a fine-tuning dataset.

The base dataset was collected while the robot end-effector followed pre-planned trajectories, namely Free-Space DataSet (FSDS). FSDS was designed to train the Neural Network for foundational force/torque sensing ability, and therefore, it includes random manual contacts measured by an F/T sensor at the end-effector throughout the data collection process. FSDS serves as the backbone of the training set, as it provides the model with unbiased information. Specifically, the robot's motion is independent of the wrench, ensuring comprehensive coverage of the robot's dynamics.

The fine-tuning dataset should be collected considering potential model application scenarios. We collected two dataset, namely Contact Sliding DataSet (CSDS) and Hand-Guiding DataSet (HGDS), to optimize model performance for these particular tasks. In contrast to the base dataset, the fine-tuning datasets generally exhibit two characteristics: (i) The trajectories are not pre-planned smooth trajectories but real-time evaluated trajectories arising from control laws, which

often include noisy measurements and various uncertainties. (ii) The robot motions are highly coupled with the external forces. For instance, friction force always resists the direction of sliding in hybrid force control tasks, and the end-effector fully complies with the external wrench during hand-guiding.

Although our experiments indicate that the model fine-tuned with one task, e.g., hand-guiding, can effectively be applied to another task, e.g., contact sliding, with considerable accuracy, we aim to mitigate any potential bias by identifying the skewed information.

### B. Training Data Collection

The data collection and experiments presented in the following sections were conducted using the Denso-VS060, a 6-axis position-controlled industrial robot. During FSDDS and HGDS collection, a 3D-printed sphere with a diameter of 50mm was used as the end-effector. For CSDDS collection, an aluminum cylinder pin with a diameter of 20mm was used. Both end-effectors were mounted on the F/T sensor.

1) *Free-space DataSet (FSDDS)*: The collection procedure commenced by sampling multiple random end-effector positions within the workspace. Each position was assigned random roll, pitch, and yaw angles selected within the specified ranges. A trajectory planner then determined the shortest trajectory between each point sequentially. During the execution of these pre-planned trajectories, forces were manually and continuously applied to the end-effector in a random manner. Given that Denso VS060 provides only joint position measurements, we obtained joint velocity and acceleration through the first and second derivatives of joint position. To marginally reduce signal noise, we employed a third-order Butterworth Filter, yet some noise was retained, positing that NN models should train on noisy signals for improved resilience. The training data, which incorporates F/T sensor readings, joint current, position, velocity, and acceleration, was recorded for FSDDS and all subsequent datasets under 100Hz system frequency.

2) *Contact Sliding DataSet (CSDDS)*: CSDDS was generated through direct end-effector contacts with a steel plate, which was secured within the FSDDS workspace. Multiple contact points were randomly sampled in the specified area. For each contact point, the end-effector repeated the following: (i) Making contact with the plate at a random angle and applying a desired force for 30 seconds. To induce disturbances, a random reference force was sampled within the range of 4N to 30N every 0.2 second. (ii) Sliding towards the next contact point while maintaining the applied force. (iii) Disengaging from the plate after reaching the next contact point.

Fig. 6 illustrates that the contact force was controlled through an admittance control scheme in the workspace. Sliding motions parallel to the plate followed the pre-planned straight trajectories between points, and therefore, sliding friction was not actively controlled. Using the Inverse Kinematics Model, we can evaluate the commanded joint positions from the desired X, Y, and Z coordinates.

The CSDDS collection should be repeated for multiple contact planes in order to cover a possibly large portion of the workspace. However, achieving this may require a flexible

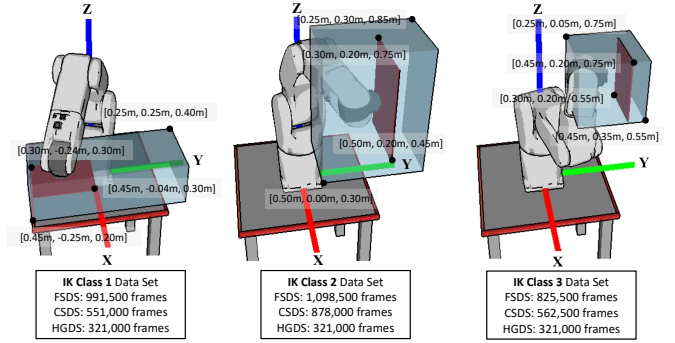


Fig. 3: Visualization of the data region for three workspaces with three different IK Classes. The transparent blue box and opaque red plane indicate the bounding boxes and location of the fixed plates, respectively. The postures of Denso show the center of the nearest joint position clusters, or IK solutions, based on which the data was collected.

experimental setup that allows for adjustable plane locations and orientations. The ideal setup for full-range data collection would involve two robots pushing against each other to simulate in-contact effects. Alternatively, the contact plate could be mounted to the robot's end-effector, enabling programmable plane locations and trajectories. Due to the constraints of the setup, we collect CSDDS data on fixed contact planes.

3) *Hand-Guiding DataSet (HGDS)*: HGDS was generated when the robot executed a hand-guiding task, where the end-effector responded compliantly to external force measurements. The same admittance control law in Fig. 6 was utilized but applicable to the three-dimensional workspace.

### C. Training Data Visualization

We collected the training data considering three dissimilar Inverse Kinematics Classes (IK Classes). each IK Class incorporates their respective FSDDS, CSDDS, and HGDS. Fig. 3 provides a visualization of the IK Classes' postures and the corresponding workspace regions in an OpenRave simulated environment. The figure also shows the Cartesian coordinates of the workspace, contact plane, as well as the total number of data frames used for training. The velocity distribution of the training data is shown in Fig. 4, suggesting that all datasets were collected under low-speed scenarios. Due to the limited space, we show only the distribution of Joint 1, 2, and 3 in FSDDS and CSDDS. The remaining datasets show similar characteristics as the data being displayed.

## V. MODEL TRAINING AND COMPARISON

When a lightweight NN model is trained with a large dataset, it tends to underfit the training data, resulting in inaccurate estimation. To address this issue, we propose enlarging the hidden layers or increasing the network depth to capture higher non-linearity and diversities introduced by dissimilar IK Classes. However, instantaneous wrench feedback is crucial in real-time tasks, particularly high-precision force-control tasks such as assembly. The challenge arises when using a large neural network model, as it can lead to longer inference

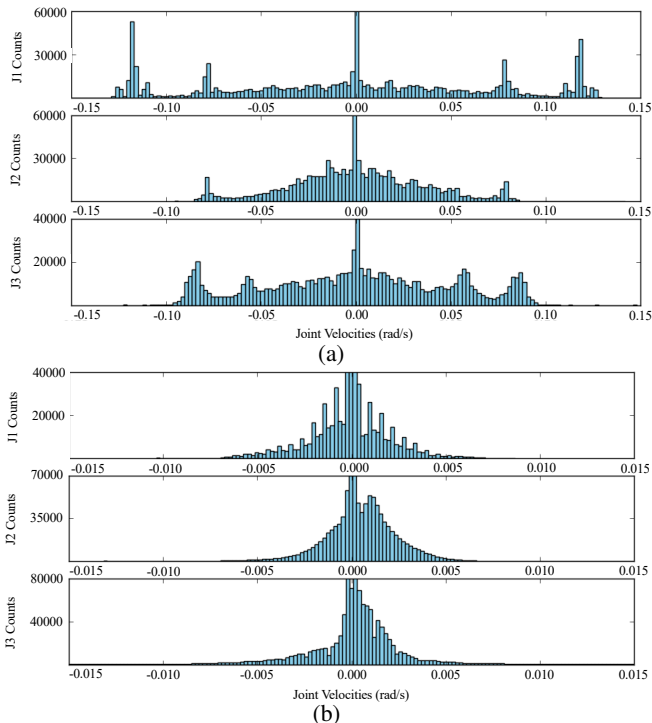


Fig. 4: Velocity distribution of Joint 1, 2, and 3 in (a) FSDS; (b) CSDS shown in histograms.

times. In general industrial application scenarios, additional computational resources such as GPUs can be costly. Thus, there is a tradeoff between the model size and inference time that needs to be considered, taking into account the expected performance of the model in applications.

To understand the relationship between training data coverage and model behaviors, and to optimize the model size for applications, we experimented with different model sizes using the FSDS from either a single IK Class or all IK Classes. Specifically, we trained the proposed MLP, LSTM, and CNN models by using the following parameters: (i) MLP model with two hidden layers and three candidate layer sizes: 256, 512, 1024; (ii) LSTM model with FC layers each comprising 256 neurons, input length of 100, and two candidate hidden state size: 128, 256; (iii) CNN model with two convolutional layers consisting of 3 and 6 channels, 5x5 convolution kernels, and two FC layers each comprising 512 neurons.

The quantized error, evaluated on the test set of 150,000 frames, is shown in Table I. As we expand the size of hidden layers, the estimation accuracy tends to improve across all dimensions. However, this also leads to an increased inference time. Notably, smaller models shows a significant decrease in accuracy when encompassing all three IK Classes, whereas the impact on larger models is less evident.

The tested CNN model displays a higher RMSE compared to both the MLP and LSTM models, even with its significant computational cost. The MLP and LSTM models, having similar inference times, exhibit nearly equivalent RMSE values and demonstrate consistent drops in accuracy across all IK Classes. We favored the MLP structure for two main reasons: (i) The recurrent nature of the LSTM can result in inconsistent estimations, where a steady input may yield drifting outputs,

Test Set RMSE (N for F; Nm for T)							
Model	Datasets	Fx	Fy	Fz	Tx	Ty	Tz
CNN	1	4.09	4.52	6.80	0.30	0.31	0.19
CNN	1,2,3	4.46	4.98	7.52	0.38	0.38	0.23
LSTM HS256	1	2.86	2.68	3.69	0.17	0.19	0.08
LSTM HS128	1	3.15	2.95	4.04	0.19	0.21	0.08
LSTM HS256	1,2,3	3.04	2.97	4.70	0.20	0.21	0.08
LSTM HS128	1,2,3	3.40	3.36	5.21	0.21	0.23	0.09
MLP LS1024	1	<b>2.48</b>	<b>2.22</b>	<b>3.39</b>	<b>0.15</b>	<b>0.17</b>	<b>0.06</b>
MLP LS512	1	2.90	2.61	3.64	0.17	0.19	0.07
MLP LS256	1	3.68	3.37	4.45	0.23	0.25	0.08
MLP LS1024	1,2,3	2.60	2.44	3.47	0.17	0.18	0.07
MLP LS512	1,2,3	3.28	3.00	4.56	0.20	0.21	0.08
MLP LS256	1,2,3	4.30	3.89	5.33	0.26	0.31	0.09

Inference Time					
	CNN	LSTM 256	MLP 256	MLP 512	MLP 1024
Time	1.95ms	2.21ms	0.20ms	0.88ms	2.43ms

TABLE I: RMSE on the same test set and model inference time. ‘LS’ and ‘HS’ stand for hidden Layer Size for MLP and hidden state size for LSTM. ‘Datasets’ suggests the datasets involved in training.

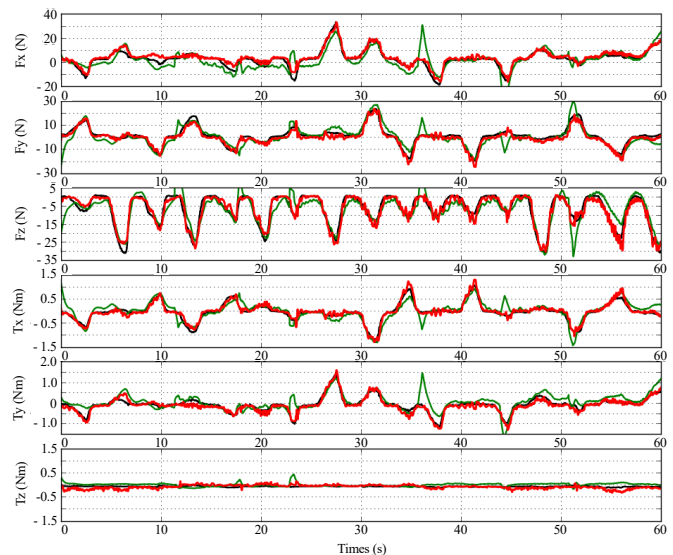


Fig. 5: Comparison between the NN-estimated (red), GMO-estimated (green) and measured wrench (black) for random pre-planned free-motion trajectories.

potentially undermining its reliability; and (ii) The MLP implementation is more straightforward. In conclusion, for all subsequent control tasks in our experiments, we utilized an MLP model with 2 hidden layers, each having 1024 neurons.

## VI. EXPERIMENTAL APPLICATIONS

### A. Wrench Estimation in Free Motion

The free-motion experiment served as an online test set to evaluate the performance of the trained model. Test trajectories were randomly generated and forces were applied following the same manner as FSDS collection for IK Class 1. The NN model used in this experiment was trained with only FSDS.

In Fig. 5 and Table II, we compare the estimations from the proposed method, GMO, and sensor measurements. It’s evident that while the implemented GMO could capture the force variation in this low-speed scenario, its overall accuracy

Model	Fx	Fy	Fz	Tx	Ty	Tz
Proposed	2.17	2.22	2.28	0.09	0.12	0.08
GMO	5.22	4.12	5.62	0.20	0.27	0.10

TABLE II: RMSE for the free-motion online test.

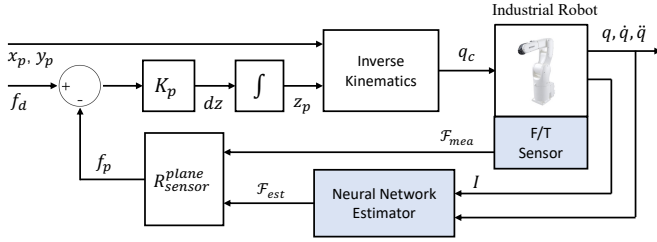


Fig. 6: Block diagram for force control on contact planes.  $x_p$ ,  $y_p$ , and  $z_p$  are the end-effector coordinate in the plate’s frame.  $f_d$ ,  $f_p$ ,  $I$  and  $R_{sensor}^{plane}$  indicate the desired force on the plate, the sensed or estimated force, the joint current, and the frame transformation matrix.

is unsatisfactory. In contrast, the proposed method consistently delivers promising results, showing both close alignment with the measurements in the Figure and low RMSE values.

### B. Force Control for In-contact Spiral Sliding

We employed an in-contact spiral sliding experiment to highlight the benefits of fine-tuning a model for specific applications. The end-effector traced a predetermined spiral trajectory on a fixed-position plate. Instead of depending on the F/T sensor for control feedback, we leveraged the estimation from the NN model, which was initially trained by FSDDS and subsequently fine-tuned by CSDDS. Fig. 6 provides the block diagram of the closed-loop control.

In the experiment, the end-effector initially moved towards the plate, then applied constant force of 20N at a contact angle of 10 degrees. Subsequently, it slid along a spiral trajectory once the force was stabilized. Fig. 7 provides a visualization of the experiment and Table III shows the RMSE comparison. The effect of force control can be interpreted from the Z-axis force. Despite the exclusion of spiral trajectories from the CSDDS, the fine-tuned model still achieved accurate wrench estimation by learning from simple straight sliding trajectories.

In contrast, both the base model and GMO show reduced accuracy, particularly during contact when the robot remains static from 3s to 8s. In the sliding phase, both methods exhibit significant peak errors, with joint 6 being notably affected. These inaccuracies can be caused by the robot’s extreme low-speed operation, leading to the prominent hysteresis issue for our robot model. The same issue also accounts for the large peak errors displayed in Fig. 5, taking place during speed inversion. Addressing these hysteresis errors often requires a non-local memory of robot states [14]. The enhanced performance of the fine-tuned model in tackling this issue can be attributed to two primary factors: (i) CSDDS is a dataset collected under this specific low-speed scenario, capturing trajectories rich in hysteresis, and (ii) Admittance control in the workspace typically results in coupled joint motion, thereby coupled hysteresis. An NN model can inherently discern these

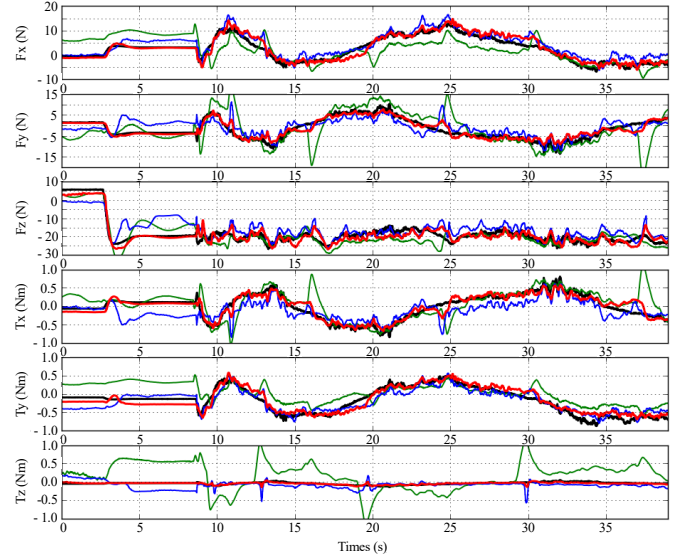


Fig. 7: Comparison between the fine-tuned model (red), base model (blue), and GMO (green) estimations with the measured wrench (black) for in-contact spiral sliding.

Model	Fx	Fy	Fz	Tx	Ty	Tz
CSDDS Fine-tuned	1.60	1.67	2.37	0.12	0.12	0.02
FSDDS Trained	2.43	3.49	4.82	0.26	0.16	0.11
GMO	4.33	5.73	3.74	0.28	0.32	0.41

TABLE III: RMSE for the in-contact spiral sliding experiment.

coupling patterns, which is often overlooked in conventional model-based methods that assess joint frictions separately.

### C. Sensorless Hand-guiding

We employ the HGDS in this study to fine-tune the base model for enhanced hand-guiding performance. Again, the HGDS is notably biased, as joint motions consistently align with the end-effector forces due to the compliant nature of the hand-guiding task. On the other hand, this straightforward motion pattern elucidates why a smaller HGDS (comprising 321,000 data frames, in contrast to the 991,500 frames in the FSDDS) yields such a significant improvement in accuracy upon fine-tuning the base model. This observation is evident in Fig. 8, wherein both the base model and GMO occasionally miss peak values, while the fine-tuned model consistently predicts values closely aligned with the ground truth. A quantitative comparison is presented in Table IV, suggesting that the estimation error is halved through the fine-tuning process.

### D. Force/Torque Control for Tight Assembly

In addition to the in-contact sliding task, the estimator’s reliability was further validated by successfully completing a widely-recognized industrial task: tight assembly [32], [33]. Precise control over forces and torques in all directions is essential for pin insertion. This task requires highly accurate force sensing with minimal time delay.

In this experiment, a pair of aluminum pin and hole with diameters of 20mm and 0.1mm clearance were used. The

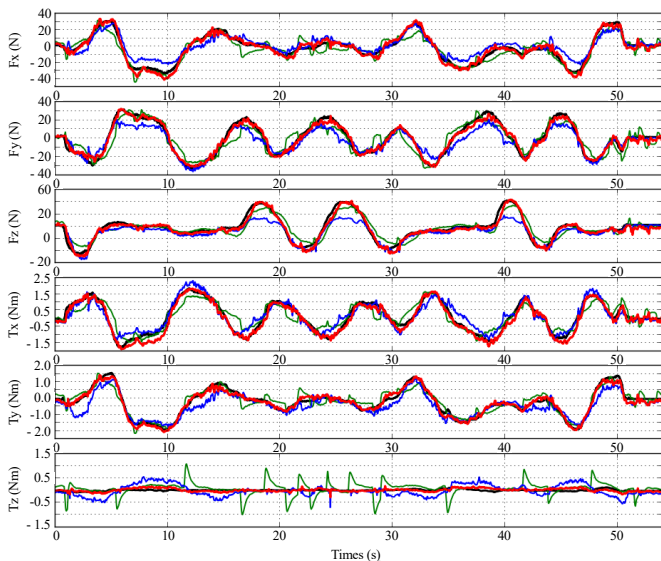


Fig. 8: Comparison between the fine-tuned model (red), base model (blue), and GMO (green) estimations with the measured wrench (black) in hand-guiding.

Fig. 8 RMSE (N for F; Nm for T)						
Model	Fx	Fy	Fz	Tx	Ty	Tz
CSDS Fine-tuned	3.29	3.07	4.25	0.22	0.15	0.07
FSDS Trained (base)	6.85	6.87	9.88	0.32	0.36	0.23
GMO	6.11	7.28	8.63	0.42	0.29	0.28

TABLE IV: RMSE for the hand-guiding experiment.

hole was placed within the workspace for IK Class 1, and the pin was attached to the F/T sensor using a coupling. The NN-estimated wrench was used for control instead of the measurements. The insertion process began 3mm above the hole, with a 2mm center and  $5^\circ$  orientation misalignment.

By setting the reference force in the pin-tip frame to  $[0N, 0N, 5N, 0Nm, 0Nm]$  and leaving the end-effector twist uncontrolled for the cylinder pin, a three-phase insertion process can be anticipated, depicted in Fig. 9. Initially, the pin moved downward until making contact. Following this, due to the zero reference force and torque in the XY directions, the pin automatically aligned both its center and orientation with the hole. In the final phase, the pin continued its insertion, making fine adjustments to its orientation. For this phase, another controller set with smaller gains was employed, taking into account the tight clearance and rigid environment that could result in high-magnitude force oscillations.

During the insertion phase, the pin made multi-point contact with the hole. This presents a scenario where identical end-effector torques can result in different torques at the joints, based on the number of contact points. For example, in a single-point contact situation, the torques perceived at the end-effector get amplified by the robot link when transmitted to the joints, leading to significant current variations. Conversely, when there are two-point contacts in opposite directions, no amplification occurs, resulting in only a subtle change in the joint current measurement. Given the presence of noise, the NN model often struggles to capture these slight variations, thus compromising accuracy during the insertion phase. Such

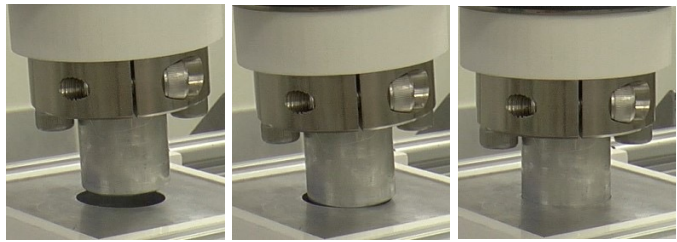


Fig. 9: Three-phase insertion procedure involving descending, aligning, and inserting.

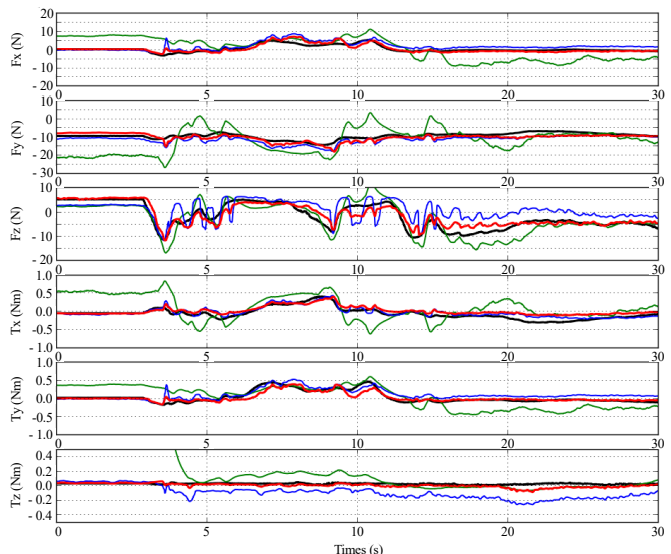


Fig. 10: Comparison between the fine-tuned model (red), base model (blue), and GMO (green) estimations with the measured wrench (black) in the pin insertion task.

an issue is particularly challenging to identify near certain robot configurations, such as singularities.

To tackle this problem, we collected additional training data by having the robot execute the pin insertion task at various locations within the workspace. This Pin Insertion DataSet (PIDS) contains 95,500 data frames. We haven't addressed this dataset in Section IV since it was specifically designed for IK Class 1 and confined to limited areas. Following this, we fine-tuned the model using both CSDS and PIDS, which subsequently achieved an insertion depth of 18mm, as shown in Fig. 10. Using only the CSDS to fine-tune the base model would cause the pin to get stuck at 12mm. The CSDS+PIDS fine-tuned model demonstrated reasonable accuracy during the initial 7 seconds when the pin had single-point contact with the hole. However, it still presented a relatively large error during the multi-contact phase due to the aforementioned issue.

## VII. CONCLUSION

In this paper, we propose an approach to estimating the end-effector wrench with Neural Networks. The model takes the joint currents and states as input and estimates the external wrench in real-time. It avoids using embedded joint torque sensors and can replace 6-axis end-effector F/T sensors in industrial applications. The implemented model has demonstrated high estimation accuracy and stability across differ-

Model	F <sub>x</sub>	F <sub>y</sub>	F <sub>z</sub>	T <sub>x</sub>	T <sub>y</sub>	T <sub>z</sub>
CSDS+PIDS Fine-tuned	1.07	1.67	2.03	0.10	0.08	0.04
FSDS Trained (base)	1.94	2.15	4.56	0.08	0.11	0.15
GMO	5.53	6.75	3.19	0.34	0.25	0.39

TABLE V: RMSE for the pin insertion experiment.

ent industrial tasks, being trained with the well-categorized datasets and enhanced with the fine-tuning strategy.

All training datasets were collected under low-speed conditions, consistent with the contact-rich tasks demonstrated in this paper. Future research might explore potential challenges, including safety concerns, associated with data collection during high-speed operations. Moreover, devising a calibration scheme could enhance the method's adaptability when changing the end-effector or attaching supplementary equipment to the robot. Another promising avenue for future research is to combine the sensorless F/T estimation here with recent robust force control methods [3], which can further alleviate possible instabilities caused by estimation errors or delays. Such a combination could enable even more sensitive sensorless manipulation.

#### VIII. ACKNOWLEDGEMENT

This research was supported by the National Research Foundation, Prime Minister's Office, Singapore under its Medium Sized Centre funding scheme, Singapore Centre for 3D Printing, CES\_SDC Pte Ltd, and Chip Eng Seng Corporation Ltd.

#### REFERENCES

- [1] B. Siciliano, O. Khatib, and T. Kröger, *Springer handbook of robotics*, vol. 200. Springer, 2008.
- [2] F. Suárez-Ruiz, X. Zhou, and Q.-C. Pham, "Can robots assemble an ikea chair?," *Science Robotics*, vol. 3, no. 17, p. eaat6385, 2018.
- [3] H. Pham and Q.-C. Pham, "Convex controller synthesis for robot contact," *IEEE Robotics and Automation Letters*, vol. 5, no. 2, pp. 3330–3337, 2020.
- [4] A. De Luca and R. Mattone, "Sensorless robot collision detection and hybrid force/motion control," in *Proceedings of the 2005 IEEE international conference on robotics and automation*, pp. 999–1004, IEEE, 2005.
- [5] M. Van Damme, P. Beyl, B. Vanderborcht, V. Grosu, R. Van Ham, I. Vanderniepen, A. Matthys, and D. Lefeber, "Estimating robot end-effector force from noisy actuator torque measurements," in *2011 IEEE International Conference on Robotics and Automation*, pp. 1108–1113, IEEE, 2011.
- [6] A. Wahrburg, J. Bös, K. D. Listmann, F. Dai, B. Matthias, and H. Ding, "Motor-current-based estimation of cartesian contact forces and torques for robotic manipulators and its application to force control," *IEEE Transactions on Automation Science and Engineering*, vol. 15, no. 2, pp. 879–886, 2017.
- [7] S. K. Kommuri, S. Han, and S. Lee, "External torque estimation using higher order sliding-mode observer for robot manipulators," *IEEE/ASME Transactions on Mechatronics*, vol. 27, no. 1, pp. 513–523, 2022.
- [8] D. Nguyen-Tuong, M. Seeger, and J. Peters, "Model learning with local gaussian process regression," *Advanced Robotics*, vol. 23, no. 15, pp. 2015–2034, 2009.
- [9] X. Liu, F. Zhao, S. S. Ge, Y. Wu, and X. Mei, "End-effector force estimation for flexible-joint robots with global friction approximation using neural networks," *IEEE Transactions on Industrial Informatics*, vol. 15, no. 3, pp. 1730–1741, 2018.
- [10] A.-N. Sharkawy, P. N. Koustoumpardis, and N. Aspragathos, "Human-robot collisions detection for safe human-robot interaction using one multi-input-output neural network," *Soft Computing*, vol. 24, no. 9, pp. 6687–6719, 2020.
- [11] D. Kim, D. Lim, and J. Park, "Transferable collision detection learning for collaborative manipulator using versatile modularized neural network," *IEEE Transactions on Robotics*, 2021.
- [12] W. Khalil and E. Dombre, *Modeling identification and control of robots*. CRC Press, 2002.
- [13] A. De Luca and R. Mattone, "Actuator failure detection and isolation using generalized momenta," in *2003 IEEE international conference on robotics and automation (cat. No. 03CH37422)*, vol. 1, pp. 634–639, IEEE, 2003.
- [14] Y. Liu, J. Li, Z. Zhang, X. Hu, and W. Zhang, "Experimental comparison of five friction models on the same test-bed of the micro stick-slip motion system," *Mechanical Sciences*, vol. 6, no. 1, pp. 15–28, 2015.
- [15] S. Liu, L. Wang, and X. V. Wang, "Sensorless haptic control for human-robot collaborative assembly," *CIRP Journal of Manufacturing Science and Technology*, vol. 32, pp. 132–144, 2021.
- [16] C. Gaz, E. Magrini, and A. De Luca, "A model-based residual approach for human-robot collaboration during manual polishing operations," *Mechatronics*, vol. 55, pp. 234–247, 2018.
- [17] C. Gaz, M. Cognetti, A. Oliva, P. R. Giordano, and A. De Luca, "Dynamic identification of the franka emika panda robot with retrieval of feasible parameters using penalty-based optimization," *IEEE Robotics and Automation Letters*, vol. 4, no. 4, pp. 4147–4154, 2019.
- [18] J. Hu and R. Xiong, "Contact force estimation for robot manipulator using semiparametric model and disturbance kalman filter," *IEEE Transactions on Industrial Electronics*, vol. 65, no. 4, pp. 3365–3375, 2017.
- [19] S. Schaal, C. G. Atkeson, and S. Vijayakumar, "Scalable techniques from nonparametric statistics for real time robot learning," *Applied Intelligence*, vol. 17, no. 1, pp. 49–60, 2002.
- [20] S. Vijayakumar and S. Schaal, "Local dimensionality reduction for locally weighted learning," in *Proceedings 1997 IEEE International Symposium on Computational Intelligence in Robotics and Automation CIRA'97: Towards New Computational Principles for Robotics and Automation*, pp. 220–225, IEEE, 1997.
- [21] D. Nguyen-Tuong and J. Peters, "Local gaussian process regression for real-time model-based robot control," in *2008 IEEE/RSJ International Conference on Intelligent Robots and Systems*, pp. 380–385, IEEE, 2008.
- [22] A. Gijbberds and G. Metta, "Real-time model learning using incremental sparse spectrum gaussian process regression," *Neural networks*, vol. 41, pp. 59–69, 2013.
- [23] N. Yilmaz, J. Y. Wu, P. Kazanzides, and U. Tumerdem, "Neural network based inverse dynamics identification and external force estimation on the da vinci research kit," in *2020 IEEE International Conference on Robotics and Automation (ICRA)*, pp. 1387–1393, IEEE, 2020.
- [24] D.-H. Lee, W. Hwang, and S.-C. Lim, "Interaction force estimation using camera and electrical current without force/torque sensor," *IEEE Sensors Journal*, vol. 18, no. 21, pp. 8863–8872, 2018.
- [25] J. Xia and K. Kiguchi, "Sensorless real-time force estimation in microsurgery robots using a time series convolutional neural network," *IEEE Access*, vol. 9, pp. 149447–149455, 2021.
- [26] H. Farazi and S. Behnke, "Online visual robot tracking and identification using deep lstm networks," in *2017 IEEE/RSJ International Conference on Intelligent Robots and Systems (IROS)*, pp. 6118–6125, IEEE, 2017.
- [27] D. Wu, Y. Zhang, M. Ourak, K. Niu, J. Dankelman, and E. Vander Poorten, "Hysteresis modeling of robotic catheters based on long short-term memory network for improved environment reconstruction," *IEEE Robotics and Automation Letters*, vol. 6, no. 2, pp. 2106–2113, 2021.
- [28] I. Goodfellow, Y. Bengio, and A. Courville, *Deep learning*. MIT press, 2016.
- [29] S. Hochreiter and J. Schmidhuber, "Long short-term memory," *Neural computation*, vol. 9, no. 8, pp. 1735–1780, 1997.
- [30] T. Zhang, X. Liang, and Y. Zou, "Robot peg-in-hole assembly based on contact force estimation compensated by convolutional neural network," *Control Engineering Practice*, vol. 120, p. 105012, 2022.
- [31] Y. LeCun and Y. Bengio, "Convolutional networks for images, speech, and time series," *The handbook of brain theory and neural networks*, vol. 3361, no. 10, p. 1995, 1995.
- [32] N. Vuong, H. Pham, and Q.-C. Pham, "Learning sequences of manipulation primitives for robotic assembly," in *2021 IEEE International Conference on Robotics and Automation (ICRA)*, pp. 4086–4092, IEEE, 2021.
- [33] L. Johannsmeier, M. Gerchow, and S. Haddadin, "A framework for robot manipulation: Skill formalism, meta learning and adaptive control," in *2019 International Conference on Robotics and Automation (ICRA)*, pp. 5844–5850, IEEE, 2019.